RSC Advances

PAPER

View Article Online
View Journal | View Issue

Cite this: *RSC Adv.*, 2021, **11**, 25511

Influence of Ag nanoparticles anchored on protonated g-C_3N_4–Bi_2MoO_6 nanocomposites for effective antibiotic and organic pollutant degradation

Muniyandi Govinda raj,[a] Elayaperumal Vijayakumar,[a] Bernaurdshaw Neppolian,[b] Sandeep Kumar Lakhera[c] and Aruljothy John Bosco *[a]

The development of noble metal-anchored semiconductors for photocatalytic processes is now garnering interest for potential application to toxic pollutants as well as antibiotic degradation. Herein, we report novel Ag@p-g-C_3N_4–Bi_2MoO_6 nanocomposites synthesized by facile hydrothermal and calcination methods with a size of about 50 nm, exhibiting superior photocatalytic activity for charge separation. The resulting nanocomposites were evaluated by various physiochemical techniques such as X-ray diffraction, X-ray photoelectron spectroscopy, Fourier-transform infrared spectroscopy, scanning electron microscopy, and high-resolution transmission electron microscopy. The charge transfer photogenerated carriers were confirmed by photoluminescence spectra and electrochemical impedance spectroscopy. The anchoring of Ag nanoparticles over p-g-C_3N_4/Bi_2MoO_6 decreased the band gap energy from 2.67 to 2.48 eV, to exhibit an abnormal increase in absorption of light towards the visible light region. The degradation performance of the nanocomposites in terms of antibiotic ciprofloxacin and rhodamine B degradation efficiency was measured 85 and 99.7% respectively. The superoxide radical anion $^{\bullet}O_2^-$ played a significant role throughout the entire degradation process. Focusing on the probable mechanism based on the desirable results, the present work follows the heterostructure mechanism. Moreover, this work features the feasible applications of Ag@p-g-C_3N_4–Bi_2MoO_6 as a modified photocatalyst in the treatment of both domestic and industrial waste water.

Received 10th April 2021
Accepted 1st July 2021

DOI: 10.1039/d1ra02800f

rsc.li/rsc-advances

1. Introduction

Currently, there is a great demand for natural resources worldwide mainly due to environmental degradation and pollution.[1] To resolve this issue, the provision of alternative renewable energy sources is required. Solar energy harvesting has received extensive attention in the fields of photocatalysis and energy storage applications.[2,3] Due to the rapid development of industrial and human activities most of the carcinogenic dyes from tannery industries get passed directly into water, thereby resulting in environmental pollution.[4–6] Among them, ciprofloxacin (CIP), $C_{17}H_{18}N_3O_3$, belongs to the second-generation fluoroquinolone antibiotic family mainly composed of quinolone structure and a piperazine moiety.[7] CIP is extensively used in various fields, such as medicine, livestock and agriculture. Due to the metabolic activities, CIP has a negative impact on human health and the environment. To overcome these issues, antibiotics are being replaced by environmentally friendly and renewable technology. Photocatalysis offers an alternative solution for the complete degradation of antibiotics by boosting reaction conditions.[8–14]

Most of the traditional methods used for wastewater treatment have recently suffered due to them receiving less attention in environmental remediation, particularly anaerobic oxidation layer partition and adsorption.[15,16] To overcome this issue, the use of a noble metal-based semiconductor photocatalyst has been found to be the most efficient and viable technique to degrade macromolecular contaminants into less harmful and non-toxic compounds. In general, an enormous number of semiconductor metal oxide and sulfide photocatalysts, including TiO_2, ZnO, WO_3, CdS, In_2S_3, and Ag_3PO_4, have been bench-marked for photocatalytic activity through the efficient degradation of organic pollutants.[17,18]

It is well known that polymeric graphitic carbon nitride (g-C_3N_4) with a layered 2D structure has a broad range of

[a]*Department of Chemistry, SRM Institute of Science and Technology, Kattankulathur, 603203, Chennai, Tamilnadu, India. E-mail: johnbosa@srmist.edu.in; sambosco@gmail.com; Tel: +91-9840757430; +91-8610498493*

[b]*Energy and Environmental Remediation Lab, SRM Research Institute, SRM Insitute of Science and Technology, Kattankulathur, 603 203, Chennai, Tamilnadu, India*

[c]*Department of Physics and Nanotechnology, SRM Institute of Science and Technology, Kattankulathur, 603203, Chennai, Tamilnadu, India*

applications in materials chemistry due to its flexible physical and chemical properties and tunable electronic structure, showing outstanding potential for visible-light active photocatalysis.[19,20] Besides this, g-C_3N_4 contains abundant functional groups such as carbon (C) and nitrogen (N), which augment the material properties to boost its broad specific area housing active absorption sites for organic pollutants.[21,22] Meanwhile, there have been few attempts on investigating noble metals anchored on heterojunction semiconductors to reduce the band gap energy. Indeed, g-C_3N_4 has certain limitations in realistic photocatalysis applications, such as inadequate real surface area, less separation of photoexcited electron–hole pairs, limited electron transfer, poor quantum yield, and low light-harvesting ability. Promoting the efficiency of g-C_3N_4 by doping with transition metals (*e.g.*, Cu, Co, and Ag) and non-metal components (*e.g.* P, S, I, O, and B) not only improves the density of both donor and acceptor, but also facilitates the transport of electrons and increases the visible-light absorption at an appropriate wavelength.[23–26] In recent reports the aurivillius metal oxide group is generally represented by the formula $Bi_2X_{n-1}Y_nO_{3n+3}$ (X = Ca, Sr, Ba, Pb, Na and Y = Ti, Nb, Ta, Mo, W) and is considered to be the most popular and active photocatalyst owing to its layered structures and outstanding photoelectrical properties. Bismuth molybdate (Bi_2MoO_6) consists of interlaced $[Bi_2O_2]^{2+}$ and perovskite group (MoO_4^{2-}) layers.[27] The foremost virtues of pure Bi_2MoO_6 are those such as lower band gap energy nearly equal to 2.4–2.8 eV, nontoxicity and low cost, and it showed an improved light response compared with wide-band-gap window photocatalysts such as TiO_2 and ZnO. Moreover, pristine Bi_2MoO_6 suffers from a wide range of problems in large-scale practical applications, like poor separation of charge transfer, low quantum efficiency and scarce energetic sites.[28–30] To resolve these disadvantages, numerous endeavors have been adopted involving modifying doping techniques.[31]

Considering the above key points, we are interested in synthesizing composites of Ag nanoparticles anchored on p-g-C_3N_4/Bi_2MoO_6 surface *via* a facile and straightforward hydrothermal method. As is evident, Ag nanoparticles affixed on the surface layer of p-g-C_3N_4/Bi_2MoO_6 can further improve the photoinduced charge carriers mainly due to surface plasmon resonance.[32] Furthermore in comparison with bare g-C_3N_4/Bi_2MoO_6, decorating Ag nanoparticles on p-g-C_3N_4/Bi_2MoO_6 could enhance the photocatalytic degradation of various contaminants such as CIP and rhodamine B (RhB) under visible light irradiation, measured at around 85% and 99.7%, respectively, within 60 min.

2. Experimental

2.1 Materials

All reagents used in the present work were of analytical grade and used without further purification. Ultrapure water was used in all the experiments. Melamine (99%), bismuth(III) nitrate pentahydrate, ammonium molybdate tetrahydrate, CIP, and RhB were purchased from Sigma-Aldrich, India. HCl (37 wt%) and ethanol used as solvents for synthesis were obtained from Avra Chemicals, India.

2.2 Synthesis of g-C_3N_4

For pristine g-C_3N_4, a modified procedure was adopted from a previous publication.[33] Firstly, melamine was ground into fine powder with a mortar and pestle. The fine powder was transferred into an alumina boat crucible and kept for calcination at 550 °C at a ramp rate of 5 °C min^{-1} for 4 h. After the reaction was cooled to ambient temperature, the final yellow product was crushed and named as g-C_3N_4.

2.3 Synthesis of protonated g-C_3N_4 or p-g-C_3N_4

Typically, 1 g of bulk g-C_3N_4 was dissolved in 25 mL of 3 M HCl and stirred for 12 h at room temperature. After the completion of the reaction, the product suspension was washed with deionized water until it was neutral. The mixture was placed in a hot-air oven for drying at 80 °C for 12 h. Finally the dried powder was obtained and labelled as p-g-C_3N_4.[33]

2.4 Synthesis of Bi_2MoO_6

Bi_2MoO_6 was synthesized by a facile hydrothermal method with slight modification.[34] About 0.485 g of $Bi(NO_3)_3 \cdot 5H_2O$ and 0.088 g of $Na_2MoO_4 \cdot 2H_2O$ were dissolved in 40 mL MilliQ-pore water under vigorous stirring for 5 h, followed by sonication for 15 min. The mixture was then transferred into a Teflon-lined stainless steel autoclave with a filling volume of 50 mL and heated up to 150 °C for 15 h. After being dried at room temperature the obtained product was washed with deionized water and absolute ethanol about three times and dried in a hot-air oven for 6 h at 80 °C. It was further annealed in a muffle furnace at 300 °C for 3 h (temperature ramp rate: 5 °C min^{-1}).

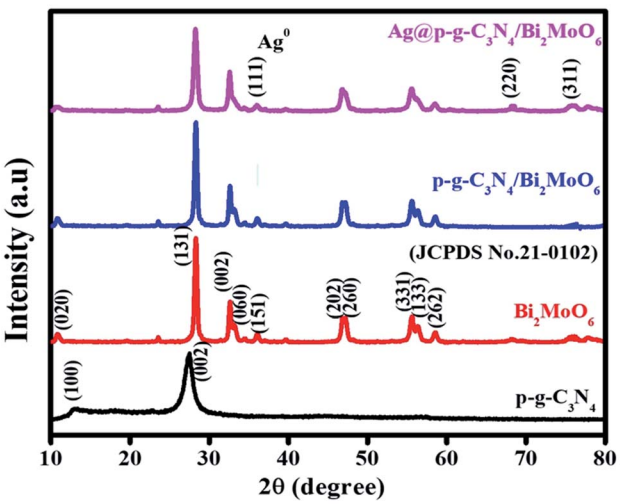

Fig. 1 XRD patterns of the prepared p-g-C_3N_4, Bi_2MoO_6, p-g-C_3N_4/Bi_2MoO_6, and Ag@p-g-C_3N_4/Bi_2MoO_6 photocatalysts.

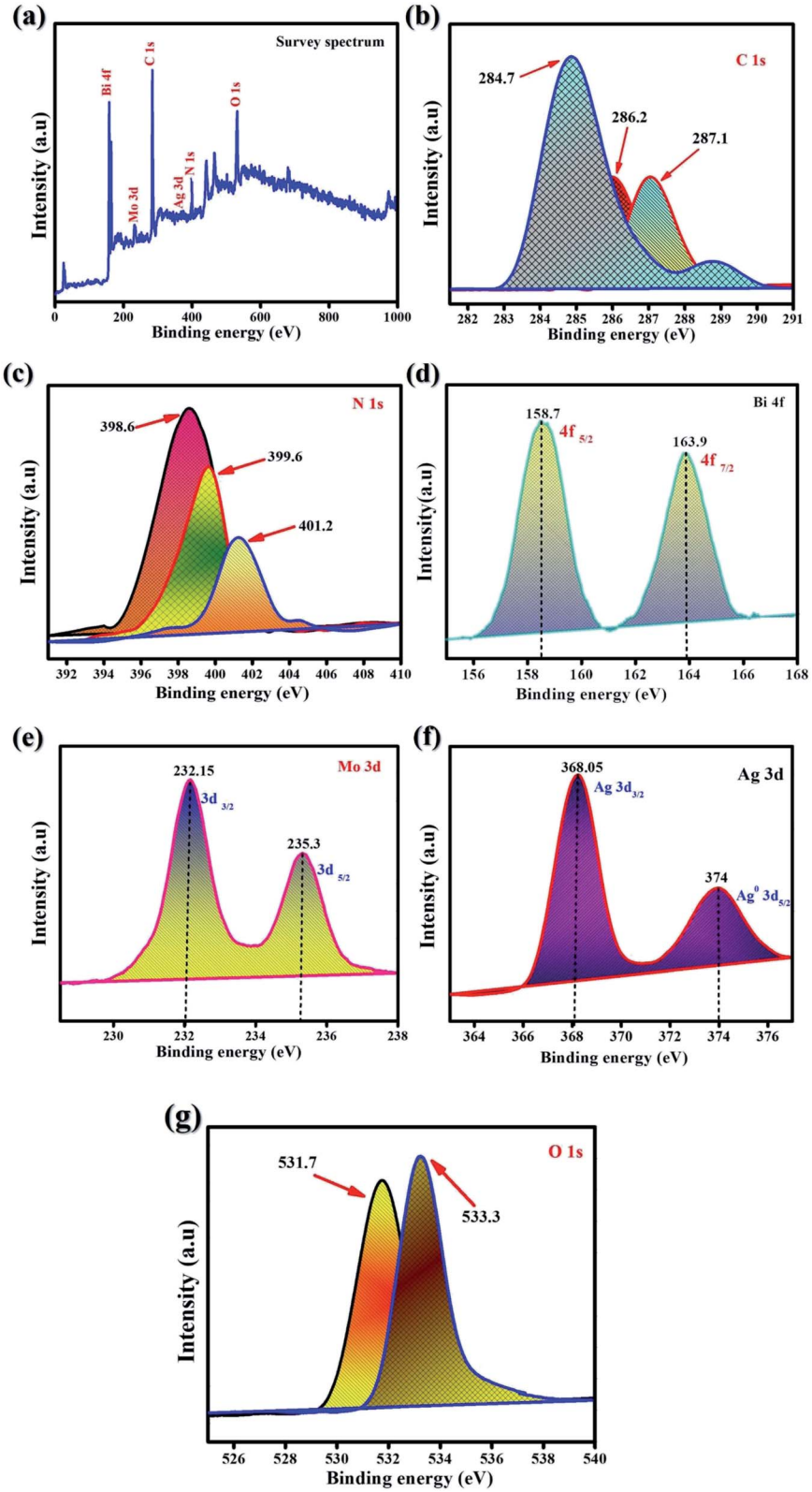

Fig. 2 XPS spectra of the as-synthesized Ag@p-g-C_3N_4/Bi_2MoO_6. (a) Survey scan, (b) C 1s, (c) N 1s, (d) Bi 4f, (e) Mo 3d, (f) Ag 3d, and (g) O 1s.

2.5 Synthesis of p-g-C_3N_4/Bi_2MoO_6 and Ag@p-g-C_3N_4/Bi_2MoO_6

To fabricate the Ag-loaded nanocomposites, 100 mg of p-g-C_3N_4 was dissolved in 40 mL of deionized water and stirred for 30 min followed by the dropwise addition of 1 : 2 stoichiometric ratio of 0.485 g of $Bi(NO_3)_3 \cdot 5H_2O$ and 0.088 g of $Na_2MoO_4 \cdot 2H_2O$. The solution was kept under vigorous magnetic stirring for 30 min. After that, for loading Ag into the bulk solution, prior as-weighed $AgNO_3$ (0.0424 g) was added to above the mixture. Then, the solution was ultrasonically treated for 15 min under vigorous magnetic stirring for 1 h. It was then transferred into a Teflon-lined stainless steel autoclave of 50 mL capacity and heated up to 150 °C for 15 h. The obtained final product was centrifuged and washed with distilled water and absolute ethanol to remove the impurities and dried at 80 °C for 6 h. After drying, the samples were further annealed in a muffle furnace at 300 °C for 3 h (temperature ramp rate: 5 °C min^{-1}). The obtained powder sample was denoted as Ag@p-g-C_3N_4/Bi_2MoO_6. For comparison, the same synthetic procedure was followed for p-g-C_3N_4/Bi_2MoO_6 but without addition of $AgNO_3$.

2.6 Materials characterization

The crystallinity of the samples was probed using the Cu K alpha line (lambda = 0.154 nm) of an X-ray diffractometer (XRD, Panalytical Xpert Pro). XRD data were taken from $2\theta = 10$ to 80° with a step size of 0.025°. The obtained diffraction patterns were compared to a reference pattern.

Morphological studies were conducted to identify the structure of Ag@p-g-C_3N_4/Bi_2MoO_6 by scanning electron microscopy (SEM). The microscopic images were obtained using a Bruker FE-SEM operating at 15 000 V with a built-in EDX setup. High-resolution transmission electron microscopic (HRTEM) imaging and EDS elemental mapping were carried out with a JEOL 2010F TEM with an accelerating voltage of 200 kV. To confirm the chemical composition and oxidation state of the materials, X-ray photoelectron spectroscopy (XPS) was performed with a Physical Electronics System India, using Al Kα radiation as the excitation source. The obtained resultant binding energy values from XPS were calibrated with carbon peak as background reference. Fourier transform infrared spectroscopy (FTIR) was conducted with a Perkin Elmer instrument (USA) in the range of 4000 to 400 cm^{-1}. The optical band gap and charge separation efficiency of the synthesized catalyst were analyzed by UV-visible DRS with $BaSO_4$ as the background (Evolution 220 PC spectrophotometer). Photoluminescence (PL) analysis was performed with a Fluorolog (Horiba Yvon) spectrophotometer. A lamp source was used in the photocatalytic performance investigation (Xe lamp, 300 W). The transient photocurrent response of all of the synthesized samples was investigated on an electrochemical workstation using a general three-electrode setup (Shanghai Chenhua CHI-660D).

2.7 Photocatalytic experiments

The photodegradation of RhB dye and CIP antibiotic as model pollutants was investigated using a 300 W Xe lamp, with a UV cut-off filter (λ > 400 nm). Typically, 50 mg of Ag@p-g-C_3N_4/Bi_2MoO_6 photocatalyst was dispersed in 50 mL of pollutant solution (concentration of 10 ppm) and placed in a Pyrex reactor. For 30 min, the solution was stirred under dark condition to reach the adsorption–desorption equilibrium state for the solution. At regular intervals of 10 min, an aliquot of 4 mL was extracted at a particular time after visible light irradiation and the concentration of CIP antibiotic and RhB dye was determined by measuring the absorbance corresponding to their respective wavelengths (λ_{max}) of 278 and 554 nm that was analyzed by a UV-visible spectrophotometer (Specord-200 plus UV-visible spectrophotometer, Germany). The photocatalyst and the remaining pollutant were separated using centrifugation. Furthermore, for recycling experiments, the photocatalyst cycling ability was investigated by analyzing the removal of CIP after the sequential running of four cycles. To identify the mineralization rate in the pollutant, total organic carbon (TOC) was measured using an analyzer (Shimadzu TOC-L instrument, Japan). Additionally, a trapping experiment was used to determine the significant active species involved in the degradation of the antibiotic. Different scavengers (concentration of 5 mM), namely benzoquinone (BQ), ethylenediaminetetraacetic acid disodium (EDTA-2Na), and isopropyl alcohol (IPA), were added into the CIP solution as scavengers of superoxide anion radicals, holes, and hydroxyl radicals, respectively.

3. Results and discussion

3.1 XRD analysis

Powder XRD studies were used to investigate the crystalline structure of the as-prepared samples (p-g-C_3N_4, Bi_2MoO_6, p-g-C_3N_4/Bi_2MoO_6 and Ag@p-g-C_3N_4/Bi_2MoO_6). As seen in Fig. 1 the pristine p-g-C_3N_4 displays two distinct peaks at $2\theta = 12.08°$ and 27.8°, which are due to the interplanar stacking corresponding to the tri-triazine groups [100] and [002] of the aromatic laminate plane, well matched to the standard JCPDS (87-1526)

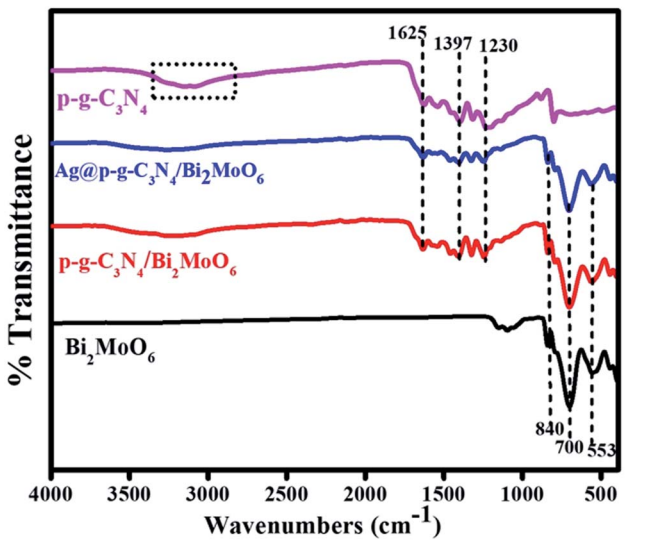

Fig. 3 FTIR spectra of p-g-C_3N_4, Bi_2MoO_6, p-g-C_3N_4/Bi_2MoO_6, and Ag@p-g-C_3N_4/Bi_2MoO_6.

values.[35,36] The XRD patterns are clearly defined to validate the orthorhombic crystalline structure of γ-BMO (JCPDS no. 21-0102). The diffraction peaks of Bi_2MoO_6 were observed in the pattern of p-g-C_3N_4/Bi_2MoO_6 composites, suggesting that heterojunctions were successfully established. The peaks of p-g-C_3N_4 of (100) and (002) phases were found to be invisible and overlapped with the (131) peak of Bi_2MoO_6. The characteristic diffraction peaks of Ag at $2\theta = 32.7$, 46.8, 55.7, and 67.9° suggest the (111), (200), (220), and (311) planes were observed for Ag-doped p-g-C_3N_4/Bi_2MoO_6 composites perfectly matching JCPDS no. 02-1067.[37] Simultaneously, the rest of the major diffraction peaks of Bi_2MoO_6 show that Ag nanoparticles are decorated on the p-g-C_3N_4/Bi_2MoO_6 heterojunction.

3.2 XPS analysis

XPS was performed to analyze the valency states and all chemical species of the synthesized samples. Fig. 2 presents the survey spectrum of all of the characteristic elements of carbon, nitrogen, bismuth, molybdenum, oxygen, and silver. Fig. 2a shows the XPS survey spectrum of as-synthesized samples of Ag@p-g-C_3N_4/Bi_2MoO_6. Fig. 2b shows the two distinct XPS peaks of C 1s, which could be attributed to amorphous carbon of graphite C–C bonds appearing at 284.7 and 287.1 eV. For p-g-C_3N_4 composite, the binding energies at 398.6 eV, 399.9 eV and 401.2 eV are observed for the N 1s spectrum as shown in Fig. 2c and fine characteristic peaks are attributed to C–N–C coordination. Bi 4f is detected *via* the signal as shown in Fig. 2d at consistent binding energies of 158.7 eV (Bi $4f_{5/2}$) and 163.9 eV

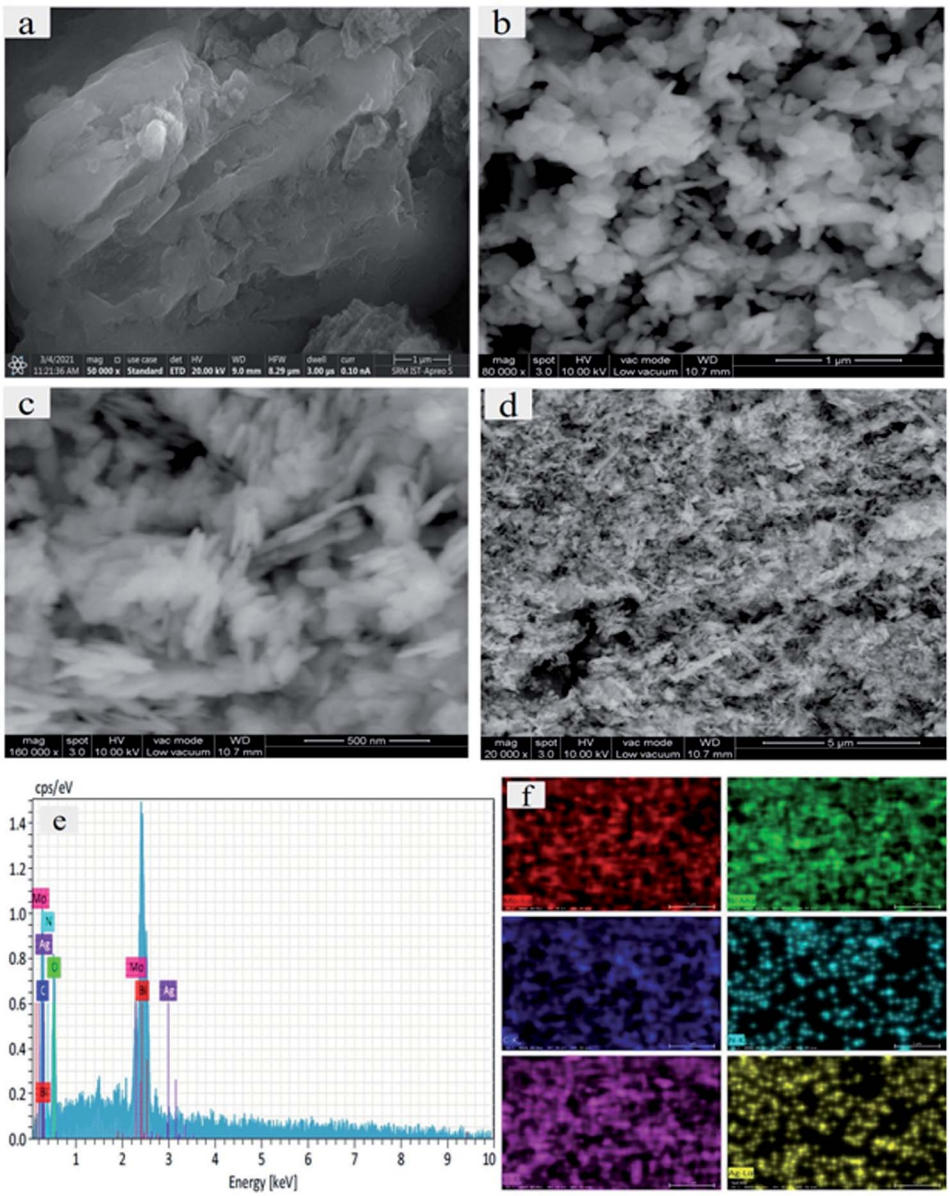

Fig. 4 (a–d) SEM images of as-synthesized samples: (a) p-g-C_3N_4, (b) Bi_2MoO_6, (c) p-g-ssC_3N_4/Bi_2MoO_6 and (d) Ag@p-g-C_3N_4/Bi_2MoO_6. (e) Elemental composition of Ag@p-g-C_3N_4/Bi_2MoO_6. (f) Elemental maps of Ag@p-g-C_3N_4/Bi_2MoO_6.

(Bi $4f_{7/2}$), attributed to Bi metallic compound. The characteristic spin-orbital splitting of photoelectrons for Mo^{6+} oxidation state in the 3d orbital, particularly in $d_{5/2}$ and $d_{3/2}$, corresponds to the binding energy peaks in the range of 232.1 and 235.3 eV corresponding to individual Mo atoms that co-exist in different chemical states as shown in Fig. 2e The standard peaks of Ag 3d can be found in the elemental silver metal state as shown in Fig. 2f, the peaks at 367.8 and 374 eV corresponding to the Ag $3d_{3/2}$ and Ag $3d_{5/2}$ orbital regions, respectively. In comparison, the influential O 1s peaks can be seen in Fig. 2g at 531.7 and 533.3 eV, which is compatible with the MoO_6 functionalization of Ag@p-g-C_3N_4/Bi_2MoO_6 nanocomposites.[38,39]

3.3 FTIR spectroscopy analysis

The presence of functional groups for as-prepared samples was further analyzed by FTIR. Fig. 3 shows the two pure sharp peaks at 800 cm^{-1} confirming the presence of bending mode of S-triazine in CN heterocycles. The peaks at 1230–1625 cm^{-1} were assigned to the stretching vibrations of C≡N. Moreover, the large bands at 1230, 1317 and 1397 cm^{-1} could be assigned to stretching vibration mode of C–N bond in the aromatic moiety. The peak at 1625 cm^{-1} corresponds to the stretching vibration mode of heptazine group. Additionally, the broad band at 3000–3500 cm^{-1} was ascribed to stretching mode of uncondensed amine N–H groups in g-C_3N_4. The pure Bi_2MoO_6 composite characteristic peaks at 553 and 700 cm^{-1} show the asymmetric and stretching vibration mode of the oxygen atoms in MoO_6.[40] The sharp bands at 700 and 840 cm^{-1} were attributed to the Mo–O stretching vibration mode in an octahedral structure.

3.4 SEM analysis

The surface morphologies and microstructural elemental composition of the as-prepared samples were further examined

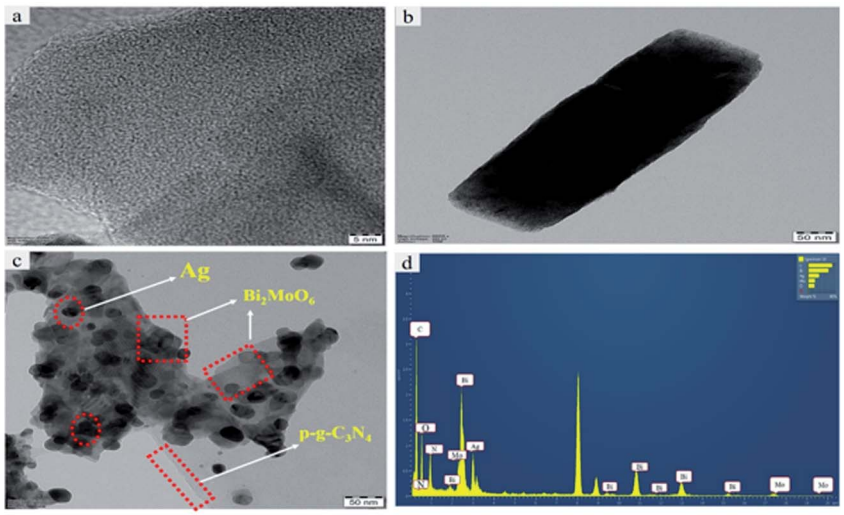

Fig. 5 Typical TEM images of (a) pristine p-g-C_3N_4, (b) Bi_2MoO_6, and (c) Ag@p-g-C_3N_4/Bi_2MoO_6. (d) EDX spectrum of Ag@p-gC_3N_4/Bi_2MoO_6.

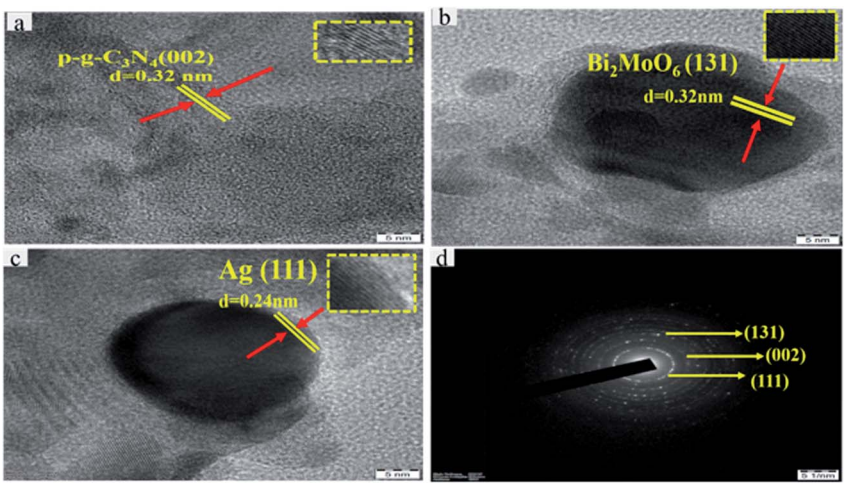

Fig. 6 HRTEM images of (a) p-g-C_3N_4, (b) Bi_2MoO_6, and (c) Ag. (d) Selected area electron diffraction pattern for Ag@p-g-C_3N_4/Bi_2MoO_6.

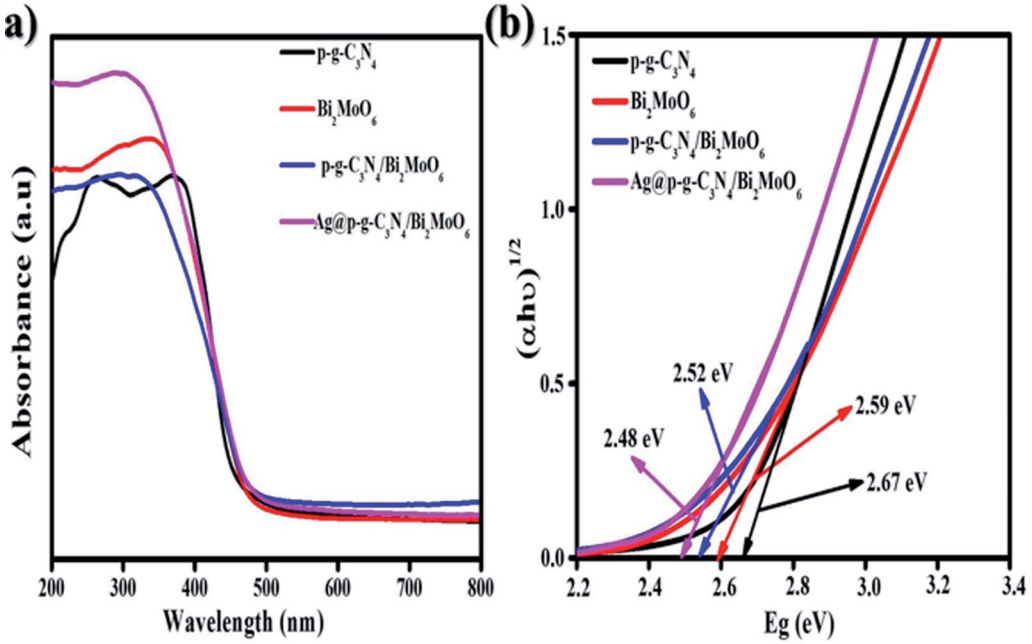

Fig. 7 (a) UV diffuse reflectance spectra and (b) graph of $(\alpha h\nu)^{1/2}$ *versus* energy (eV) of the as-synthesized Ag@p-gC_3N_4/Bi_2MoO_6 photocatalyst.

by SEM. Fig. 4a–d displays a large surface area of p-g-C_3N_4 wrinkled 2d morphology doping with p-g-C_3N_4/Bi_2MoO_6. Fig. 4a depicts the ultrathin uniform bulk layer of pristine p-g-C_3N_4. Notably, the pure Bi_2MoO_6 micro-petals with an irregular plate-like microstructure are shown in Fig. 4b. Moreover, the micro-plate combination of both p-g-C_3N_4 and Bi_2MoO_6 nanocomposites is shown in Fig. 4c. Interestingly, Fig. 4d shows the final composite of Ag nanoparticles anchored on p-g-C_3N_4 and Bi_2MoO_6 thereby confirming that some amount of Ag nanoparticles were loaded into the heterostructure, sufficiently enhancing the photocatalytic activity. Interestingly the final catalyst Ag@p-g-C_3N_4/Bi_2MoO_6 shows a rice husk-like morphology. Fig. 4e shows the EDS spectrum of the final compositions of the prepared nanocomposites. This also indicates that all of the elements C, N, Mo, Bi and Ag are present in the final composition, and the heterostructure of Ag@p-g-C_3N_4/Bi_2MoO_6 had been effectively fabricated. Fig. 4f shows the elemental mapping of Ag@p-g-C_3N_4/Bi_2MoO_6, with all the elements being present in the final composition.

3.5 TEM analysis

To further investigate the final heterostructured surface morphology, TEM was carried out for synthesized p-g-C_3N_4, Bi_2MoO_6 and Ag@p-g-C_3N_4/Bi_2MoO_6 nanocomposites as

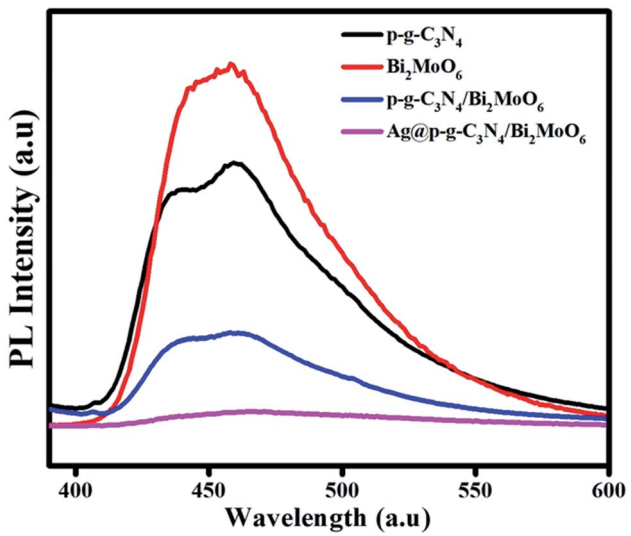

Fig. 8 PL spectra of p-g-C_3N_4, Bi_2MoO_6, p-g-C_3N_4/Bi_2MoO_6, and Ag@p-g-C_3N_4/Bi_2MoO_6.

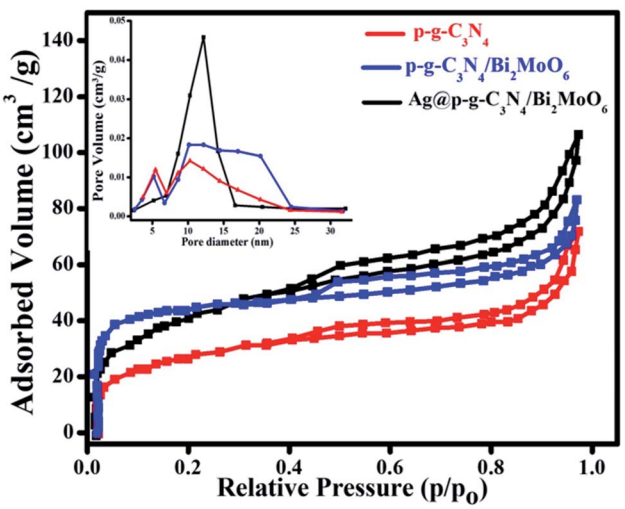

Fig. 9 N_2 adsorption–desorption isotherms and the corresponding (inset) pore-size distribution curves for as-prepared nanocomposites.

depicted in Fig. 5. As illustrated in Fig. 5a the TEM image of p-g-C_3N_4 shows a layered nanosheet, with an average thickness of 6–10 nm. Fig. 5b reveals a lower magnification image of Bi_2MoO_6 nanopetal. It is worth noting that Fig. 5c shows a close-up view of dark spot highlighted in red of Ag enwrapped with nanoplates of Bi_2MoO_6 and p-g-C_3N_4 nanosheet, which strongly confirms the formation of Ag@p-gC_3N_4/Bi_2MoO_6. Fig. 5d confirms the EDX spectrum for Ag@p-g-C_3N_4/Bi_2MoO_6. This clearly shows that all the chemical components of Ag@p-g-C_3N_4/Bi_2MoO_6 derived rice husk composites contain Ag, Bi, C, N, O, and Mo elements. Furthermore, HRTEM images of pure p-g-C_3N_4, Bi_2MoO_6, and Ag@p-g-C_3N_4/Bi_2MoO_6 are displayed in Fig. 6. It is clear from Fig. 6a that the boxed area shows the interplanar spacing lattice fringes of about 0.32 nm corresponding to the (002) facets of p-g-C_3N_4 and is in good agreement with the XRD pattern. Similarly Fig. 6b displays the selected part of Bi_2MoO_6 highlighted in red color. It also shows the interplanar spacing lattice fringes of about 0.32 nm corresponding to the (131) plane of Bi_2MoO_6. Likewise, Fig. 6c shows the interplanar spacing lattice fringes of about 0.240 nm corresponding to the (111) plane of Ag. The selected area electron diffraction pattern in Fig. 6d reveals selected discrete spots indexed to (131), (002) and (111) of the planes corresponding to Ag@p-g-C_3N_4/Bi_2MoO_6.

3.6 UV-visible diffuse reflectance spectroscopy analysis

To examine the absorption ranges and optimum energy band gaps of the synthesized nanocomposites, the optical absorption was examined from 200 to 800 nm, as shown in Fig. 7a. The p-g-C_3N_4 exhibited a moderate absorption edge around 435 nm while the bare Bi_2MoO_6 showed a steep absorption edge that is found to be 470 nm. When p-g-C_3N_4 was intercalated with Bi_2MoO_6, outstanding peaks were observed in the region of 550 nm and the absorption edges became steeper due to p-g-C_3N_4 intercalation properties. After loading Ag nanoparticles onto the surface of p-g-C_3N_4/Bi_2MoO_6, the absorption edge exhibited higher absorption intensities than that for bare p-g-C_3N_4, Bi_2MoO_6, and p-g-C_3N_4/Bi_2MoO_6. From the DRS studies it can be clearly understood that incorporating Ag onto p-g-C_3N_4/Bi_2MoO_6 extends the light absorption into the visible region thus contributing to the great potential for photocatalytic degradation. The energy gaps were determined using Tauc plots of $\alpha h\nu = A(h\nu - E_g)^{1/2}$ *versus* photon energy as shown in Fig. 7b, where α = absorption coefficient, h = Planck's constant, ν = light frequency and E_g = band gap energy. With the excellent agreement of the curve the obtained band gap energy (E_g) value was evaluated at 2.48 eV. The final catalyst was found to possess a direct band gap based on a literature survey.[41]

3.7 Photoluminescence spectra analysis

The PL emission spectra of pure p-g-C_3N_4, Bi_2MoO_6 and combinations of p-g-C_3N_4/Bi_2MoO_6 and Ag@p-g-C_3N_4/Bi_2MoO_6 catalysts were recorded under an excitation irradiation wavelength of 400 nm as shown in Fig. 8. PL is an important technique to investigate the interfacial charge transfer and isolation of photogenerated electrons and holes in photocatalysts. A lower PL intensity of Ag@p-g-C_3N_4/Bi_2MoO_6 than pure p-g-C_3N_4 and Bi_2MoO_6 can be observed from the PL spectra. This may be due to conduction band levels of bare p-g-C_3N_4 and Ag@p-g-C_3N_4 that stand at equal positions, quickly suppressing the rate of charge carrier recombination. Besides, it is interesting to note when Ag nanoparticles were decorated on the surface of p-g-C_3N_4/Bi_2MoO_6, this reduced the recombination rate of photogenerated electron–hole pairs and exhibited the lowest emission intensity, which greatly enhanced the photocatalytic activity due to the surface plasmon resonance effect of Ag.

3.8 BET analysis

As seen in Fig. 9, the Brunauer–Emmett–Teller (BET) technique was used to quantify the precise surface area and pore size distributions of the prepared nanocomposites under N_2 adsorption–desorption equilibrium conditions.[42] The surface area of p-g-C_3N_4, p-g-C_3N_4/Bi_2MoO_6, and Ag@p-g-C_3N_4/Bi_2MoO_6 nanocomposites was found to be 43.5, 64.2, and 98.4 $cm^3\ g^{-1}$, according to the BET analysis results. The broad surface area of the Ag@p-g-C_3N_4/Bi_2MoO_6 photocatalyst shows that the recombination rate of photogenerated charge carriers has been reduced. Furthermore, the increased pore volume and

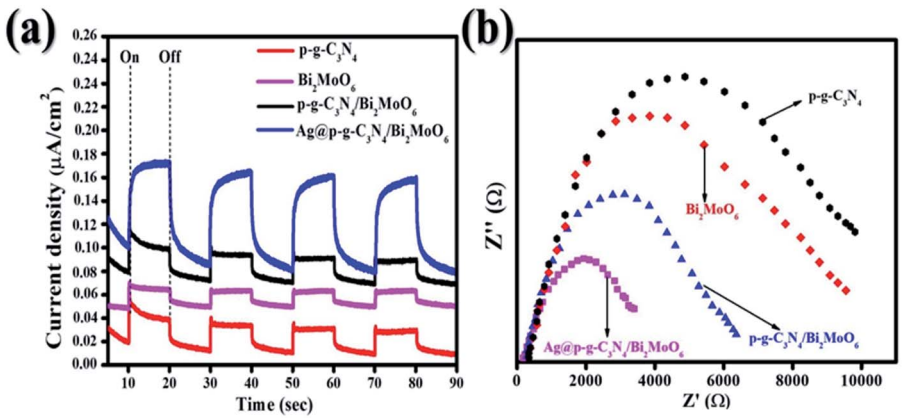

Fig. 10 (a) Transient photocurrent response of all synthesized samples and (b) EIS curves of all synthesized samples.

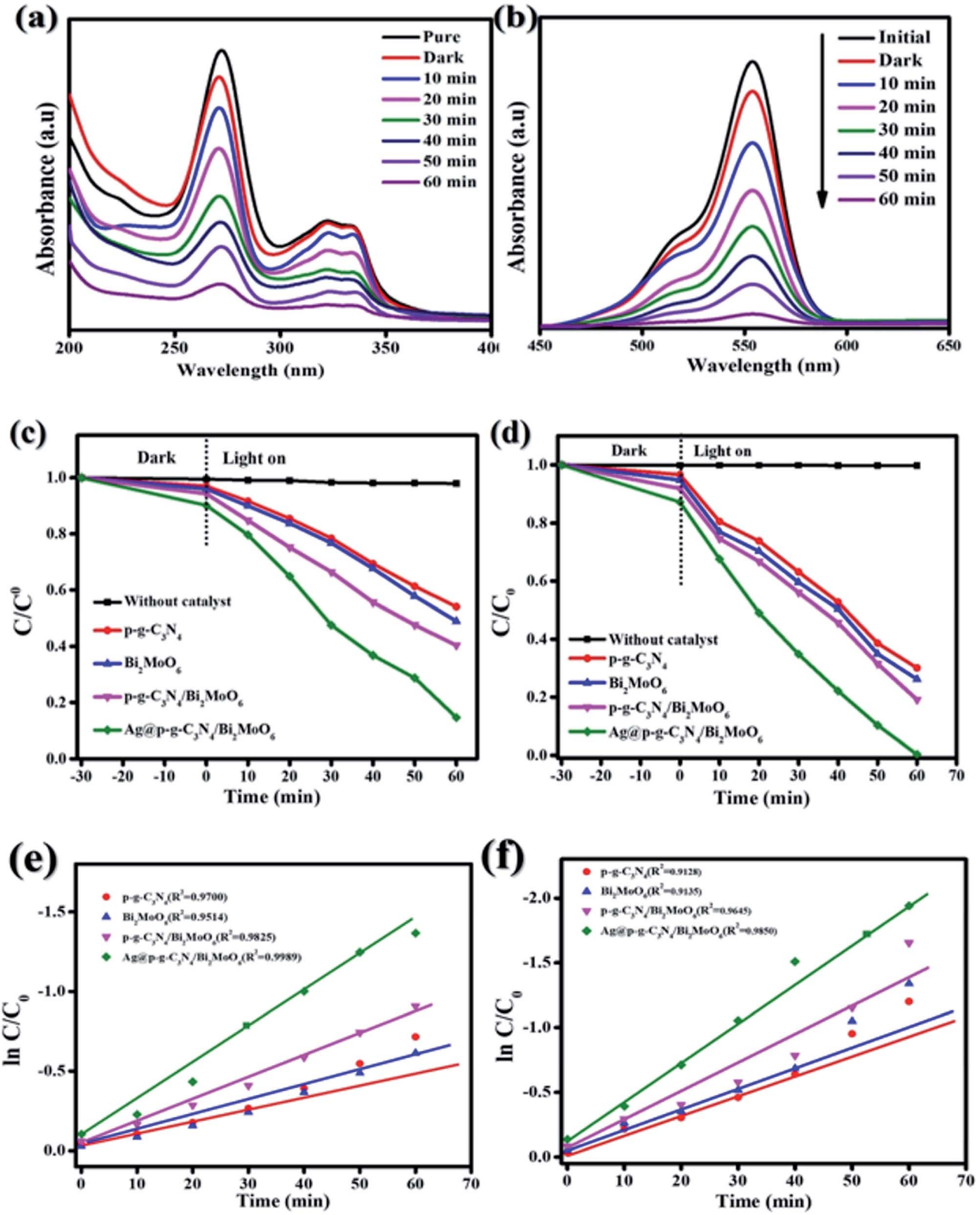

Fig. 11 (a and b) Degradation of CIP and RhB over Ag@p-g-C_3N_4/Bi_2MoO_6 nanocomposite. (c and d) Photocatalytic CIP and RhB degradation for all synthesized nanocomposites. (e and f) Corresponding kinetic plots (k_{obs}) of the as-synthesized nanocomposites.

diameter, as well as better isolation and migration of photo-generated charges, contributes to increased photocatalytic activity. As a consequence of the above results, the main Ag@p-g-C_3N_4/Bi_2MoO_6 composite is useful for improved adsorption and also provides a greater number of reactive sites for photocatalytic processes, with a major effect on photocatalytic

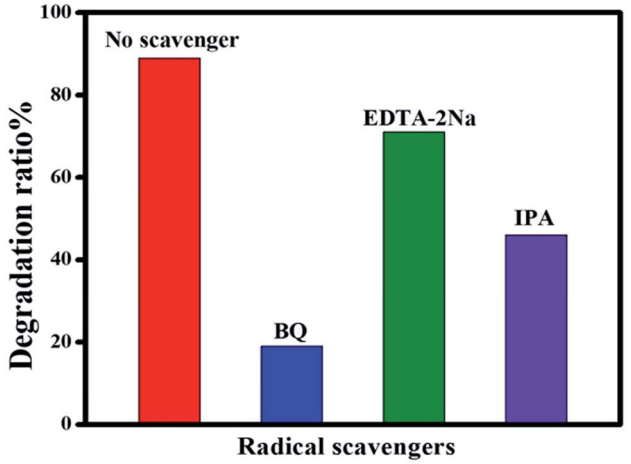

Fig. 12 Effect of scavengers on the photocatalytic degradation of CIP over Ag@p-g-C_3N_4/Bi_2MoO_6 nanocomposite.

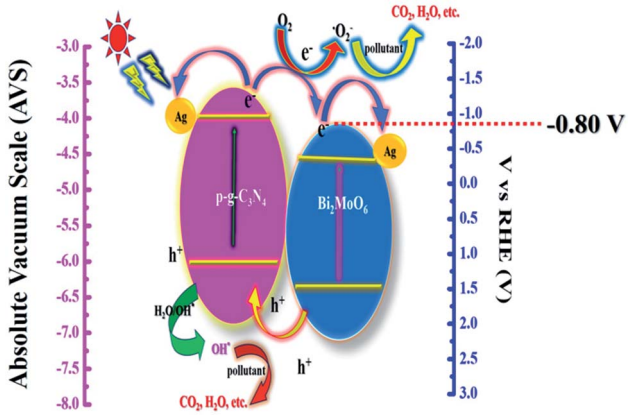

Fig. 13 Schematic representation of the probable photocatalytic mechanism for Ag@p-g-C_3N_4/Bi_2MoO_6.

efficiency development.[43,44] Importantly, in addition to the obvious increase in surface area, an increase in pore volume (inset of Fig. 9) was found, rising from 0.15 cm^3 g^{-1} for as-prepared p-g-C_3N_4 to 0.46 cm^3 g^{-1} for Ag@p-g-C_3N_4/Bi_2MoO_6, facilitating charge separation in the entire composite structure. Additionally, the addition of effective Ag and Bi_2MoO_6 components increased the pore diameter from 10.6 nm for as-prepared p-g-C_3N_4 to 15.2 nm for Ag@p-g-C_3N_4/Bi_2MoO_6.

3.9 Photoelectrochemical analysis

Photocurrent measurements and electrochemical impedance spectroscopy (EIS) are valuable methods for characterizing the separation and migration potential of photoexcited charges. As shown in Fig. 10a, the transient photocurrent measurements of Ag@p-g-C_3N_4/Bi_2MoO_6 indicate a high photocurrent density compared with pure samples, implying a more effective separation of the photoexcited charges (electron–hole pairs) and limitation of their recombination. Several repeat on–off cycles display a similar photocurrent reaction. Significantly, it shows

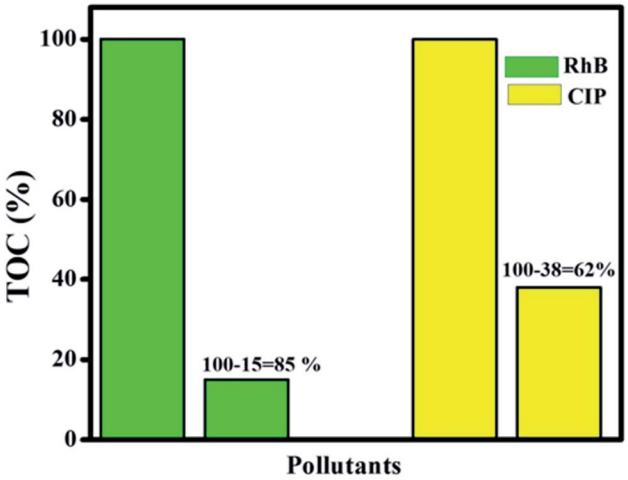

Fig. 14 Mineralization efficiency for RhB and CIP of the final Ag@p-g-C_3N_4/Bi_2MoO_6 catalyst.

that the samples have high photostability. EIS electrochemical measurements of the as-synthesized samples were also used to analyze the charge-transfer resistance between the heterostructures. Fig. 10b depicts the smaller semicircle radius of prepared nanocomposites than the pure p-g-C_3N_4 and Bi_2MoO_6. This indicates the higher efficacy in separation and charge transfer of photogenerated electron–hole pairs.

3.10 Photocatalytic performance

The photocatalytic activity of Ag@g-C_3N_4/Bi_2MoO_6 was investigated in the degradation of CIP and RhB under visible light irradiation. The results are shown in Fig. 11a and b. The results of the degradation of CIP and RhB using Ag@g-C_3N_4/Bi_2MoO_6 show excellent photocatalytic performance, with values of 85% and 99.7%, which are much higher than when using pure p-g-C_3N_4, Bi_2MoO_6 and p-g-C_3N_4/Bi_2MoO_6 combination. When pure g-C_3N_4 is used under visible light, it shows poor photocatalytic

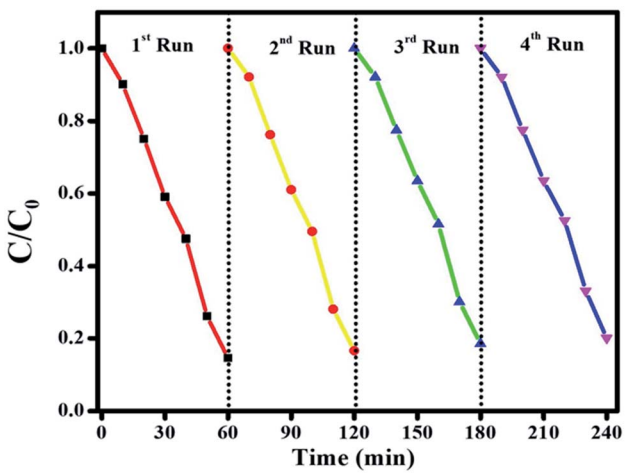

Fig. 15 The stability test for CIP degradation activity for the final Ag@p-g-C_3N_4/Bi_2MoO_6 catalyst.

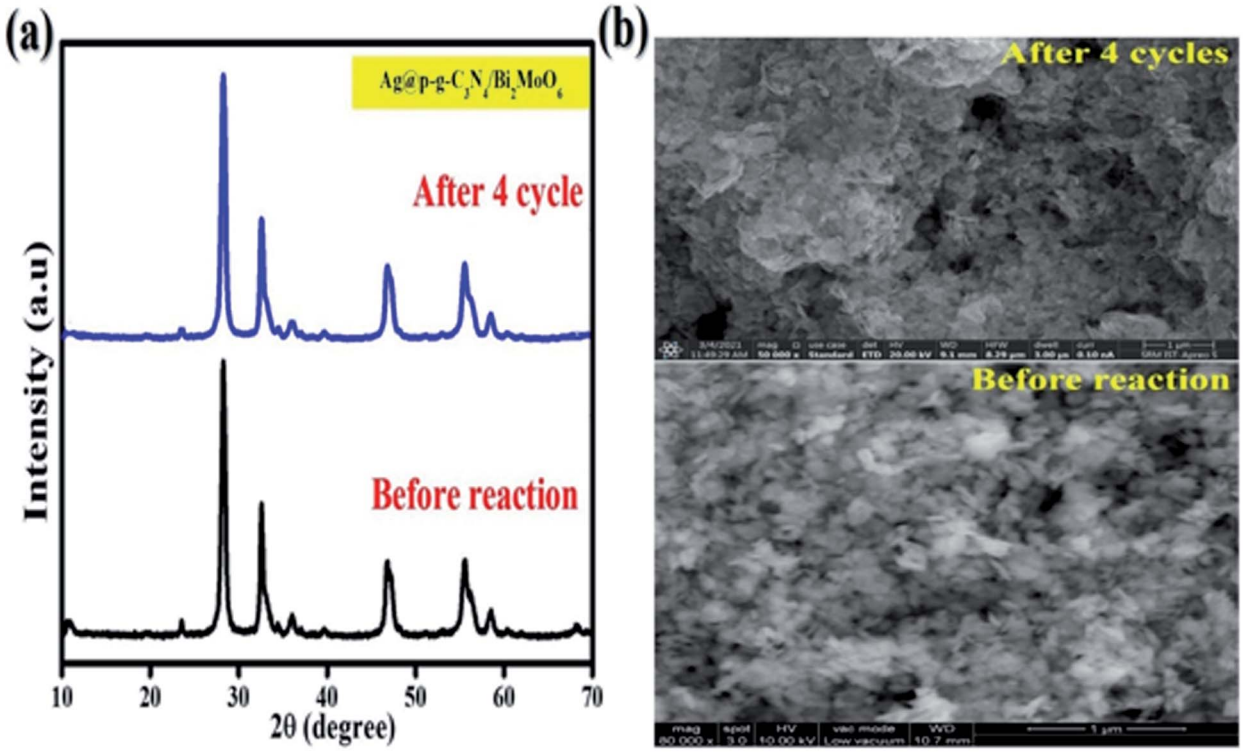

Fig. 16 (a) XRD patterns and (b) SEM images of fresh and used Ag@p-g-C_3N_4/Bi_2MoO_6 catalyst.

activity and this may be due to the inhibitory effect on the surface area of graphene sheets, while g-C_3N_4 loaded on the metallic surface of Bi_2MoO_6 would allow effective separation of the electron–hole pairs. In addition, Ag nanoparticles enwrapped on p-g-C_3N_4/Bi_2MoO_6 would further increase the photocatalytic degradation effect due to the surface plasmon resonance interaction between Ag and p-g-C_3N_4. All synthesized catalyst activities are shown in Fig. 11c and d. To understand the decomposition rate, the kinetic behavior of CIP and RhB degradation is represented as a plot of C/C_0 *versus* time (min) in accordance with the pseudo first-order reaction kinetics based on the following equation:

$$-\ln(C/C_0) = Kt$$

where C is the concentration of pollutants at time t, C_0 is the initial concentration of CIP and RhB, and K is the reaction rate constant as shown in Fig. 11e and f.

3.11 Radical trapping experiments

To identify the reactive species involved in the photodegradation of CIP, a series of radical trapping experiments were carried out using various radical scavengers. IPA was chosen as a quencher of hydroxyl radicals ($^{\bullet}OH$), EDTA-2Na was selected as a quencher of holes (h^+) and BQ was chosen as a quencher of the superoxide radical anion ($^{\bullet}O_2^-$). These quenchers were added to the photocatalyst during the degradation process. As can be seen in Fig. 12, when BQ was added into the reaction mixture the degradation rate achieved was only 19%. This clearly shows that BQ has a strong effect on CIP degradation, which demonstrates that ($^{\bullet}O_2^-$) plays an essential role in the degradation process. In contrast, the addition of IPA and EDTA-2Na has not much effect on CIP degradation, clearly indicating that (h^+) and ($^{\bullet}OH$) do not have much impact on the photocatalytic system.

3.12 Plausible degradation mechanism

The suggested photocatalytic mechanism of the synthetic heterojunctions is depicted in Fig. 13. Upon visible light irradiation, both semiconductors p-g-C_3N_4 and Bi_2MoO_6 are excited to produce photogenerated electron–hole pairs. The diagram demonstrates clearly that $^{\bullet}OH$ plays a less active role in the dye degradation process due to the band gap level of photogenerated h^+ having an energy of 2.48 V in the valence band level showing a lower energy gap than $^{\bullet}OH$ with an average energy of 2.70 V, suggesting that it is difficult for $^{\bullet}OH$ to interact from H_2O during photodegradation. It is worth noting that h^+ has a strong oxidation ability which directly decomposes the CIP molecule. More particularly, e^- at the conduction band is much smaller (−0.80 V) than that of $^{\bullet}O_2^-$ which is 1.23 V, resulting in a simple reduction of dissolved O_2 to $^{\bullet}O_2^-$ which degrades various organic matter.[45] More particularly, the decorated Ag nanoparticles used in this work play an important role in serving as a solid-state electron mediator. The e^- developed on the conduction band of p-g-C_3N_4 heterojunctions is easily transferred to Ag particles and Bi_2MoO_6 microplates, effectively promoting electron transfer and suppressing electron–hole recombination efficiency.[33] Furthermore, the formed h^+ could migrate from Bi_2MoO_6 to g-C_3N_4 in the heterojunctions, reducing recombination efficiency significantly. As a result, the photocatalytic dye degradation efficiency of Ag@p-g-

C_3N_4/Bi_2MoO_6 is higher than those of pure p-g-C_3N_4, Bi_2MoO_6, and p-g-C_3N_4/Bi_2MoO_6 composites.

3.13 TOC analysis

The TOC technique was employed to assay the mineralization of CIP and RhB using the optimum photocatalyst. Fig. 14 shows that mineralization efficiency values of 62% and 85% were achieved for CIP and RhB, respectively, while the photocatalytic efficiency values were 85% and 99.7% for CIP and RhB under 60 min of irradiation. This difference between mineralization and photocatalytic efficiency is due to the intermediates present during the photocatalytic process that can be mineralized in a longer reaction time.

3.14 Recyclability and stability

To check the stability of the photocatalyst, the recyclability is a vital parameter to determine for the final nanocomposite. Fig. 15 shows the results of stability tests for CIP degradation activity for the final Ag@p-g-C_3N_4/Bi_2MoO_6 catalyst. After 4 consecutive runs, the degradation efficiency of the catalyst was found to be 92%, which indicates the high stability of the prepared photocatalyst. For the sake of comparison, the stability of the photocatalyst was evaluated by powder XRD and SEM after four successive repeat runs and the results are displayed in Fig. 16a and b. XRD patterns and SEM images of fresh and used samples reveal that the catalyst's crystalline nature and morphological features are not destroyed after several cycles.

4. Conclusion

To conclude, we developed a simple and environmentally friendly approach of using a ternary photocatalyst, Ag@p-g-C_3N_4/Bi_2MoO_6, for environmental contaminant degradation. The unique characterization techniques revealed that the prepared Ag@p-g-C_3N_4/Bi_2MoO_6 nanocomposite possessed high purity and crystallinity. It is also to be noted that the interfacial charge separation and efficiency are fully controlled due to the formation of interfacial bonds between metallic Ag and p-g-C_3N_4/Bi_2MoO_6. Moreover, the Ag@p-g-C_3N_4/Bi_2MoO_6 catalyst shows enough durability for the degradation of CIP. Ag nanoparticles were decorated on p-g-C_3N_4/Bi_2MoO_6 which leads to a higher surface area of the photocatalyst for the photodegradation of CIP and RhB under visible light irradiation for a duration of 1 h. After four cycles, the photocatalyst maintains its effectiveness and exhibits excellent structural stability. The pollutant undergoes a pseudo first-order reaction. The mechanistic pathway suggests that ($^{\bullet}O_2^-$) plays a significant role in the photodegradation of the various pollutants. Thus, the present study demonstrates that capped Ag@p-gC_3N_4/Bi_2MoO_6 photocatalysts have a high potential for use in environmental protection.

Conflicts of interest

There are no conflicts to declare.

Acknowledgements

One of the authors, Muniyandi Govinda raj, acknowledges financial support from the University Research Fellowship (URF) SRM Institute of Science and Technology, Tamil Nadu 603 203, India. The authors gratefully acknowledge the HRTEM facility at SRMIST set up with support from MNRE (project no. 31/03/20143-15/PVSE-R&D), Government of India. We acknowledge NRC, SRM Institute of Science and Technology for providing the FE-SEM facility. The authors acknowledge the XRD facility at SRMIST set up with support from MNRE (project no. 31/03/2014-2015/PVSE-R&D), Government of India. The authors acknowledge SRM Institute of Science and Technology for providing the UV-visible DRS facility. Finally the authors are grateful for the facilities provided by the SRM Research Institute of Science and Technology. We acknowledge the Nanotechnology Research Centre (NRC), SRMIST for providing the research facilities.

References

1 L. Qin, H. Yi, G. Zeng, C. Lai, D. Huang, P. Xu, Y. Fu, J. He, B. Li, C. Zhang, M. Cheng, H. Wang and X. Liu, *J. Hazard. Mater.*, 2019, **380**, 120864.
2 Y. Fu, L. Qin, D. Huang, G. Zeng, C. Lai, B. Li, J. He, H. Yi, M. Zhang, M. Cheng and X. Wen, *Appl. Catal., B*, 2019, **255**, 117740.
3 L. Li, C. Lai, F. Huang, M. Cheng, G. Zeng, D. Huang, B. Li, S. Liu, M. Zhang, L. Qin, M. Li, J. He, Y. Zhang and L. Chen, *Water Res.*, 2019, **160**, 238–248.
4 B. Li, C. Lai, P. Xu, G. Zeng, D. Huang, L. Qin, H. Yi, M. Cheng, L. Wang, F. Huang, S. Liu and M. Zhang, *J. Clean. Prod.*, 2019, **225**, 898–912.
5 Y. Xu, B. Ren, R. Wang, L. Zhang, T. Jiao and Z. Liu, *Nanomaterials*, 2019, **9**, 10.
6 S. Li, S. Hu, W. Jiang, Y. Liu, J. Liu and Z. Wang, *J. Colloid Interface Sci.*, 2017, **501**, 156–163.
7 S. S. Imam, R. Adnan and N. H. M. Kaus, *Toxicol. Environ. Chem.*, 2018, **100**(5), 518–539.
8 L. Qin, G. Zeng, C. Lai, D. Huang, C. Zhang, P. Xu, T. Hu, X. Liu, M. Cheng, Y. Liu, L. Hu and Y. Zhou, *Sens. Actuators, B*, 2017, **243**, 946–954.
9 C. Lai, B. Li, M. Chen, G. Zeng, D. Huang, L. Qin, X. Liu, M. Cheng, J. Wan, C. Du, F. Huang, S. Liu and H. Yi, *Int. J. Hydrogen Energy*, 2018, **43**, 1749–1757.
10 J. Pei, H. Yao, H. Wang, J. Ren and X. Yu, *Water Res.*, 2016, **99**, 122–128.
11 B. Li, C. Lai, P. Xu, G. Zeng, D. Huang, L. Qin, H. Yi, M. Cheng, L. Wang, F. Huang, S. Liu and M. Zhang, *J. Clean. Prod.*, 2019, **225**, 898–912.
12 L. Qin, Z. Zeng, G. Zeng, C. Lai, A. Duan, R. Xiao, D. Huang, Y. Fu, H. Yi, B. Li, X. Liu, S. Liu, M. Zhang and D. Jiang, *Appl. Catal., B*, 2019, **259**, 118035.
13 X. Shi, Y. Li, Z. Zhang, L. Sun and Y. Peng, *Chem. Eng. J.*, 2019, **372**, 1113–1121.

14 J. Di, C. Zhu, M. Ji, M. Duan, R. Long, C. Yan, K. Gu, J. Xiong, Y. She, J. Xia and H. Li andZ. Liu, *Angew. Chem., Int. Ed.*, 2018, **130**, 15063–15067.
15 Y. Yang, C. Zhang and Z. Hu, *Environ. Sci.: Processes Impacts*, 2013, **15**, 39–48.
16 J. M. Poyatos, M. M. Muñio, M. C. Almecija, J. C. Torres, E. Hontoria and F. Osorio, *Water, Air, Soil Pollut.*, 2010, **205**, 187–204.
17 D. Chen, Y. Cheng, N. Zhou, P. Chen, Y. Wang, K. Li, S. Huo, P. Cheng, P. Peng, R. Zhang, L. Wang, H. Liu, Z. Liu and R. Ruan, *J. Clean. Prod.*, 2020, **268**, 121725.
18 E. Rahmanian, R. Malekfar and M. Pumera, *Chem. - Eur. J.*, 2018, **24**, 18–31.
19 L. Liang, Y. Cong, F. Wang, L. Yao and L. Shi, *Diamond Relat. Mater.*, 2019, **98**, 107499.
20 Y. Yang, C. Zhang, D. Huang, G. Zeng, J. Huang, C. Lai, C. Zhou, W. Wang, H. Guo, W. Xue, R. Deng, M. Cheng and W. Xiong, *Appl. Catal., B*, 2019, **245**, 87–99.
21 C. Hu, Y.-C. Chu, M.-S. Wang and X.-H. Wu, *J. Photochem. Photobiol., A*, 2017, **348**, 8–17.
22 C. Hu, Y. R. Lin and H. C. Yang, *ChemSusChem*, 2019, **12**, 1794–1806.
23 L. Shi, W. Din, S. Yang, Z. He and S. Liu, *J. Hazard. Mater.*, 2018, **01**, 010.
24 L. Yang, L. Liang, L. Wang, J. Zhu, S. Gao and X. Xia, *Appl. Surf. Sci.*, 2018, **12**, 180.
25 C. Hu, W. Z. Hung, M. S. Wang and P. J. Lu, *Carbon*, 2018, **127**, 374–383.
26 C. Zhou, D. Huang, P. Xu, G. Zeng, J. Huang, T. Shi, C. Lai, C. Zhang, M. Cheng, Y. Lu, A. Duan, W. Xiong and M. Zhou, *Chem. Eng. J.*, 2019, **370**, 1077–1086.
27 R. Guo, X. Zhang, B. Li, H. Zhang, J. Gou and X. Cheng, *J. Phys. D: Appl. Phys.*, 2019, **52**, 085302.
28 S. Wang, X. Yang, X. Zhang, X. Ding, Z. Yang, K. Dai and H. Chen, *Appl. Surf. Sci.*, 2017, **391**, 194–201.
29 Y. Liu, Z.-H. Yang, P.-P. Song, R. Xu and H. Wang, *Appl. Surf. Sci.*, 2018, **430**, 561–570.
30 Q. Liang, M. Zhang, C. Yao, C. Liu, S. Xu and Z. Li, *J. Photochem. Photobiol., A*, 2017, **332**, 357–363.
31 F. Stelo, N. Kublik, S. Ullah and H. Wender, *J. Alloys Compd.*, 2020, **829**, 154591.
32 Z. Hongru, W. Zhipan, L. Jie, K. Jun, D. Xiaoguang and W. Shaobin, *Appl. Catal., B*, 2018, **09**, 090.
33 Y. Huang, P. Wang, Z. Wang, Y. Rao, J. Cao, S. Pu, W. Ho and S. C. Lee, *Appl. Catal., B*, 2018, **08**, 078.
34 Z. Jia, F. Lyu, L. C. Zhang, S. Zeng, S. X. Liang, Y. Y. Li and J. Lu, *Sci. Rep.*, 2019, **9**, 7636.
35 Z. Chen, P. Sun, B. Fan, Q. Liu, Z. Zhang and X. Fang, *Appl. Catal., B*, 2015, **170**, 10–16.
36 S. Hu, R. Jin, G. Lu, D. Liu and J. Gui, *RSC Adv.*, 2014, **47**, 24863–24869.
37 V. Shanmugam, A. Muppudathi, S. Jayavel and K. Jeyaperumal, *Arabian J. Chem.*, 2018, **05**, 009.
38 X. Lin, D. Xu, R. Zhao, Y. Xi, L. Zhao, M. Song, H. Zhai, G. Che and L. Chang, *Sep. Purif. Technol.*, 2017, **01**, 020.
39 N. Boonprakob, N. Wetchakun, S. Phanichphant, D. Peter Sherrell, A. Nattestad, J. Chen and B. Inceesungvorn, *J. Colloid Interface Sci.*, 2014, **402**(417), 409.
40 T. Yan, Q. Yan, X. Wang, c-H. Liu, c-M. Li, S. Lu, W. Xu and M. Sun, *Dalton Trans.*, 2015, **4**, 1601–1611.
41 B. Bhanupriya, G. Rimzhim, M. M Jayant and M. Giridhar, *Nanoscale Adv.*, 2019, **1**, 2748.
42 S. Vadivel, A. L. Muppidathi, K. S. Jeyaperumal and A. Selvaraj, *J. Organomet. Chem.*, 2018, **866**, 206–213.
43 I. Papailias, N. Todorova and T. Giannakopoulou, *Catal. Today*, 2016, **280**, 37–44.
44 M. Sharma, S. Vaidya and A. K. Ganguli, *J. Photochem. Photobiol., A*, 2017, **335**, 287–293.
45 B. Bhanupriya, G. Rimzhim, M. M. Jayant and M. Giridhar, *J. Photochem. Photobiol., A*, 2019, **373**, 105–115.